Electronic supplementary information (ESI)

Efficient Two-Photon Luminescence for Cellular Imaging Using Biocompatible Nitrogen-doped Graphene Quantum Dots Conjugated with Polymers†

Ping-Ching Wu,[a] Jiu-Yao Wang,[b-d] Wen-Lung Wang,[e] Chia-Yuan Chang,[f] Chia-Hung Huang,[g,h] Kun-Lin Yang,[i] Jui-Cheng Chang,[j] Chih-Li Lilian Hsu,[d] Shih-Yao Chen,[e] Ting-Mao Chou*[k] and Wen-Shuo Kuo*[b,c,l]*

[a]Department of Biomedical Engineering, National Cheng Kung University, Tainan 701, Taiwan (R.O.C.).

[b]Allergy & Clinical Immunology Research Center, National Cheng Kung University Hospital, College of Medicine, National Cheng Kung University, Tainan 701, Taiwan (R.O.C.).

[c]Department of Pediatrics, National Cheng Kung University Hospital, College of Medicine, National Cheng Kung University, Tainan 701, Taiwan (R.O.C.).

[d]Department of Microbiology & Immunology, National Cheng Kung University Hospital, College of Medicine, National Cheng Kung University, Tainan 701, Taiwan (R.O.C.).

[e]Department of Internal Medicine, National Cheng Kung University Hospital, College of Medicine, National Cheng Kung University, Tainan 701, Taiwan (R.O.C.).

[f]Center for Micro/Nano Science and Technology, National Cheng Kung University, Tainan 701, Taiwan (R.O.C.).

[g]Metal Industries Research & Development Centre, Kaohsiung 811, Taiwan (R.O.C.).

[h]Department of Materials Science Engineering, National Cheng Kung University, Tainan 701, Taiwan (R.O.C.).

[i]Department of Biotechnology, National Kaohsiung Normal University, Kaohsiung 802, Taiwan (R.O.C.).

[j]Department of Chemical Engineering, National Cheng Kung University, Tainan 701, Taiwan (R.O.C.).

[k]Division of Plastic Surgery, Department of Surgery, E-Da Hospital, Kaohsiung 824, Taiwan (R.O.C.).

[l]Advanced Optoelectronic Technology Center, National Cheng Kung University, Tainan 701, Taiwan (R.O.C.).

*To whom correspondence should be addressed. E-mail: z9903038@email.ncku.edu.tw (S. Y. Chen), ed109842@edah.org.tw (T. M. Chou) and wenshuokuo@mail.ncku.edu.tw (W. S. Kuo).

Experimental Section

Nitrogen-doped graphene quantum dots (N-GQDs) preparation. Graphene oxide was prepared from a natural graphite powder (Bay carbon, SP-1, USA) using a modified Hummers' method.[1] Graphite (8.5 M) and $NaNO_3$ (0.6 M) (Merck, Germany) were mixed with H_2SO_4 (Wako, Japan). $KMnO_4$ (2.0 M) (J. T. Baker, USA) was slowly added with continual stirring at 35 °C overnight. Then, the ddH_2O was gradually added and continued to be stirred. Adding H_2O_2 (Shimakyu, Japan) was the method used to terminate the reaction. Washing and centrifugation with ddH_2O several times were carried out and the graphene oxide was collected. The as-prepared graphene oxide was placed in a tube furnace and heated to 400-600 °C in the presence of ammonia for 4-6 h; it was then introduced to concentrated HNO_3 (16 M) (Wako, Japan) and stirred for 2 d. The mixture was put into ultrasonicator for 2 d and then put it in oven at 160 °C for 1 d to vaporize all the liquid. Washing and centrifugation (83000 rpm) (Optima TLX Ultracentrifuge, BECKMAN, USA) with ddH_2O several times were carried out. The supernatant was collected filtered through a 0.22-μm microporous membrane. The resulting black suspension had the pH tuned to 7.4 with NaOH. The solution was remained in dialysis bags (retained molecular weight: 100kDa) overnight; the N-GQDs were obtained.

Synthesis and characterization of N-GQDs coated polymers materials (N-GQD-polymers). The positively charged polyethylenimine (PEI) (50 μg mL^{-1}) (Sigma-Aldrich Co., USA), and negative charged polystyrene sulfonate (PSS) (50 μg mL^{-1}) (Sigma-Aldrich Co., USA) were coated on the surface of negative charged as-prepared N-GQD (50 μg mL^{-1}) by the electrostatic interaction to form N-GQD-PEI and N-GQD-PEI-PSS, respectively. Centrifuging (82000 rpm) (the solutions for 20 min to remove excess polymers. The pellets (N-GQD-polymers) were re-suspended in ddH_2O, and the centrifugation process was repeated several times.

Characterization. Materials were subject to transmission electron microscopes (TEM, JEOL 1400, JEOL 2100F and JEOL 3010, Japan) observation. The height profile diagram, thickness and size of materials were determined by atomic force microscopy (AFM, multimode 8, Bruker, Germany). The crystalline structures of samples were identified using X-ray diffraction (XRD, Bruker AXS Gmbh, Germany). Fourier transform infrared spectroscopy (FTIR), ultraviolet-visible (UV-vis), zeta potential spectra and dynamic light scattering (DLS) of samples were recorded by the spectrometers: PerkinElmer RX1 USA, U-4100 Hitachi Japan and Manern Nano-ZS90 UK, respectively. Raman spectroscopy (DXR, Thermo Scientific, USA) was used to examine the crystallinity of samples with 532 nm laser. X-ray photoelectron spectroscopy (XPS, PHI 5000, VersaProbe, USA) was employed to examine the surface chemistry of the materials, the O(1s)/C(1s) and N(1s)/C(1s)

atomic ratios of materials. The photoluminescence (PL) signal was recorded by the spectrophotometer (F-7000, Hitachi, Japan).

Cell culture of human squamous carcinoma cell line (A431 cells). A431 cells were cultured in EMEM (EBSS) + 2mM Glutamine + 1% Non Essential Amino Acids + 10% Fetal Bovine Serum at 37℃ under 5% CO_2 in air. The cells were collected by trypsinization and placed onto a 10 cm tissue culture Petri dish, then allowed to grow for 2 - 4 days.

Coating antibody. The absorbance of a quantity of antibody (epidermal growth factor receptor antibody (Ab_{EGFR}) (Antagene, USA), zeta potential: 8.2 mV) was recorded by UV-vis spectroscopy (Abs: approximately 276 nm). By the electrostatic interaction, the nanomaterials were mixed with the same quantity antibody for 30 min of incubation at 4 ℃ in the dark and centrifuge (83000 rpm) to remove excess antibody; the nanomaterial-Ab_{EGFR} was prepared. On the other hand, the supernatant was retained and its absorbance measured. The difference in absorbance between the collected supernatant and the original antibody was estimated. Consequentially, the quantity of the antibody coated on the nanomaterials was calculated by Lambert-Beer's law. In the working solution of 1×PBS buffer, there was approximately 0.095 μg of Ab_{EGFR} conjugated on 1 μg of N-GQD-PEI-PSS (zeta potential of N-GQD-PEI-PSS-Ab_{EGFR}: 6.9 mV), which meant the coating efficiency was approximately 9.5%, whereas 7.8% for N-GQD (zeta potential of N-GQD-Ab_{EGFR}: 7.7 mV). In culture medium, N-GQD-PEI-PSS was approximately 9.7% for Ab_{EGFR} (zeta potential of N-GQD-PEI-PSS-Ab_{EGFR}: 7.1 mV), whereas 7.5% for N-GQD (zeta potential of N-GQD-Ab_{EGFR}: 7.4 mV). Since there is not much different between the zeta potential of nanomaterial-Ab in 1×PBS buffer and culture medium, it meant that the biomolecules would be absorbed on neither nanomaterial and Ab nor nanomaterial-Ab. In other words, the interaction among nanomaterial-Ab, Ab and cells would not be influenced by biomolecules in cultural medium, leading to no subsequently effect in the specific binding among them. Additionally, the positively charged nanomaterial-Ab was favorable for absorbance or internalization by the negatively charged surface of the cell. The above results have proven the successful absorption of Ab on the surface of materials.

Quantum yield (QY) measurement. The relative PL QY of contrast agent is the usually the ratio of the emitted photons to the absorbed photons. It can be led to

$$\mathrm{QY} = \mathrm{QY}_{\mathrm{ref}} \frac{\eta^2}{\eta_{\mathrm{ref}}^2} \frac{I}{A} \frac{A_{\mathrm{ref}}}{I_{\mathrm{ref}}} \tag{1}$$

, where QY_{ref} =0.72 is the QY of fluorescein dissolved in NaOH (0.1 M, pH 11) as a reference,[2,3] η is the refractive index of ddH_2O=1.3333, I is the integrated fluorescence intensity and A is the absorbance at the excitation wavelength. On the other hand, the absolute PL QY was also measured and estimated.[4] The absolute PL QY of N-GQD, N-GQD-PEI, and N-GQD-PEI-PSS was approximately 0.226, 0.442 and 0.573, respectively. Results were showed in **Tables 1 and 2**.

Femtosecond laser optical system for the measurements of two-photon absorption (TPA) and two-photon luminescence (TPL).[5-7] The home-made femtosecond Ti : sapphire laser optical system (repetition rate of 80 MHz) (Tsunami, Spectra-Physics, Santa Clara, CA, USA) was used in this study. ***TPA measurement.*** A femtosecond laser with a wavelength range of 720–820 nm and was used to excite TPA signals. A time-average luminescence photon count (F) is proportional to the cross section (δ) of TPA and can be given as[8]

$$F \sim \frac{1}{2}\delta\eta_2\phi C\frac{g_p}{f\tau}\frac{8nP^2}{\pi\lambda} \quad (2)$$

where η_2 is the quantum efficiency of PL, ϕ is the luminescence collection efficiency of the system, C is the concentration of the photoinitiator (For nanomaterials: the aqueous nanomaterials were put in oven overnight to vaporize the whole liquid and weighed it. Sequentially, the dry nanomaterials can be dissolved in any applicable amount of working solution.), g_p is the dimensionless quantity for degree of the second-order temporal coherence, f is the pulse repetition rate, τ is the excitation pulse width by full-width at half maximum, n is the refractive index of the measurement medium, P is the average incident power and λ is the excitation wavelength. After the SF-10 prism pair compensation, the parameters which are the collection system, the pulse repetition rate, the concentration of the materials and the excitation power can be maintained the same at different excitation wavelengths with their corresponding excitation pulse widths. On the basis of the measured excitation pulse width, the measured fluorescence photon count and the excitation wavelength, the TPA was derived as $\delta \times \eta_2$. *Via* the single photon counting module, the photomultiplier tubes (PMTs) (Hamamatsu, Japan) were used to collect the photoluminescence photon counts. The TPA can be given as

$$\delta\eta_2 \propto \lambda\tau F \quad (3)$$

An in-lab constructed autocorrelator was used to monitored the pulse widths of the different wavelengths after the objective. With 2 m ms^{-1} speed of the galvanometer scanner, the excitation spectrum was measured 720-820 nm in wavelength with 3.0 mW (this is the power before objective; the power after objective (or on sample) is 1.056 mW). The calculation will be introduced as follows) excitation power. For the all of N-GQD and N-GQD-polymers, **Fig. 2a** shows the relative TPA spectrum as function of excitation wavelength. ***Measurement of TPL spectrum***.[5,6] All of N-GQD and N-GQD-polymers were exposed to femtosecond laser, respectively. Excited wavelength: 800 nm at a power of 5.0 mW (this is the power before objective; the power after objective (or on sample) is 1.760 mW. The calculation will be introduced as follows). Scanning area 200 μm × 200 μm, frequency: 10 kHz, a duration of 1.638 s exposure time/scan= 100 μs per pixel per scan, 128 × 128 pixels/scan, pixel area= 1562.5 × 1562.5 nm^2. The focal spot area was calculated as $\pi d^2/4$, where d= 0.61 λ/NA is the full width at half maximum of the beam waist. For instance, the x-y axis focal spot (Ex: 800 nm, a 40× oil-immersion objective (*NA* 1.3)), d= 0.61*800 nm / 1.3 = 375. 38 nm; and the z axis resolution is 0.94193 μm after measurement (**Fig. S1**†). For 800 nm-excitation: t= 4.53 ms × number of scans and obtain the data. A 40× oil-immersion objective (*NA* 1.3) was used to collect the signals, and the detection range of spectrum photometer was 300-600 nm in wavelength.

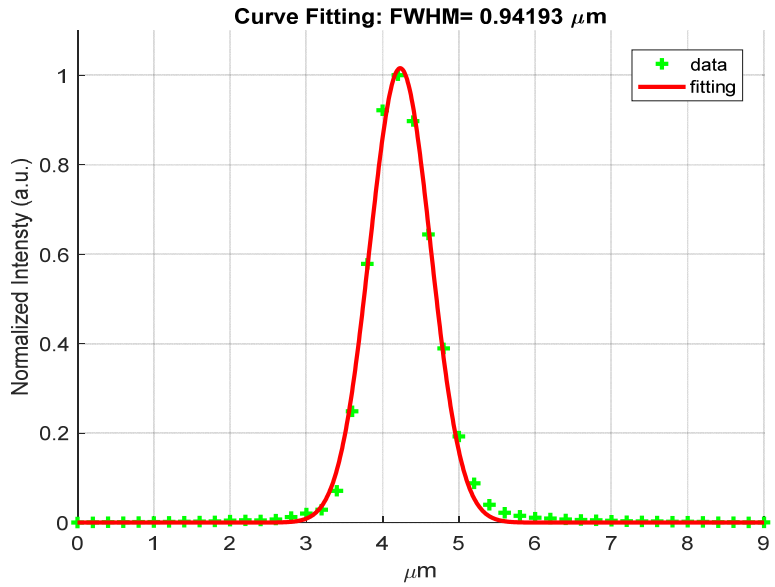

Fig. S1 According to the z axis scan of a gold thin film to measure the signal of second harmonic generation at different position, the z axis resolution of the laser system (FWHM) is around 0.94193 μm (fitting using Gaussian function).

Additionally, the calculations of laser power (mW or Joul $pixel^{-1}$) on sample were as follows. For the 40× oil-immersion objective (*NA* 1.3), the transmission rate

at 800 nm in wavelength is around 88%, and the laser power went from the output to objective would only have 40% of the original output power due to the loss of power. As a result, the calculated energy after objective (on sample) is P_{output}(mW)*40%*88%= 0.352*P_{output} (mW). For instance, P_{output} = 5.0 mW, the calculated energy after objective (on sample) is 5.0 mW*40%*88%= 1.760 mW. And if 10 kHz of scan rate (each pulse stays 0.1 ms pixel^{-1}), the calculated energy on sample (Joul pixel^{-1}) was around P_{output} (mW)*40%*88%*0.1 ms= 0.0352*P_{output} (Joul pixel^{-1}). For instance, P_{output} = 5.0 mW, the energy (Joul pixel^{-1}) on sample= 5.0 mW*40%*88%*0.1 ms= 0.176 μJoul pixel^{-1}= 176 nJoul pixel^{-1}. The power after objective (on sample) was used and marked throughput this work.

Measurement of two-photon excitation (TPE) absolute cross section. The absolute cross section of TPE was measured the luminescence signal *via* femtosecond laser optical system mentioned above. The back aperture of the 40× oil-immersion objective (*NA* 1.3) was overfilled by expansion of the laser beams. For the multiphoton excitation, the diffraction-limited illumination of the sample was approximately achieved and analyzed. Under two-photon excitation and for the thick sample limit, the relation between time-averaged luminescence photon flux $\langle F^{(n)}(t)\rangle$ and the incident power *P(t)* can be obtained. The formula can be given as[9]

$$\langle F^{(n)}(t)\rangle = \frac{1}{n}\frac{g_p^{(n)}}{(f\tau)^{n-1}}\phi\eta\sigma_n C n_0 \frac{a_n(\mathrm{NA})^{2n-4}\langle P(t)\rangle^n}{8\pi^{3-n}\lambda^{2n-3}} \tag{4}$$

, where n is the number of photons absorbed (n = 2 for the TPE), f is the laser repetition rate, τ is the laser pulse width, ϕ is the system collection efficiency, η is the luminescence quantum efficiency (or QY), C is the concentration of the fluorophore (For nanomaterials: the aqueous nanomaterials were put in oven overnight to vaporize the whole liquid and weighed it. Sequentially, the dry nanomaterials can be dissolved in any applicable amount of working solution. For reference: the reference powder can directly be weighed and dissolved in any applicable amount of working solution.), and λ is the excitation wavelength in vacuum, σ_n is the n-photon absorption cross section, and a_2 = 64 for TPE. $g_p^{(n)}$ is the n^{th}-order temporal coherence of the excitation source. Due to the limitation of resource we currently have, $\langle F^{(n)}(t)\rangle$ is temporarily not able to be calculated and the values could be replaced by the integrated TPL intensity with the symbol of *Counts*. As a result, the equation for action cross section ($\eta\sigma_2$) is turned into[10]

$$\eta\sigma_2 = \frac{\text{counts}}{\frac{1}{2}\frac{g_p^{(2)}}{f_\tau} n_0 \phi C \frac{8\langle P(t)\rangle^2}{\pi\lambda}}$$

(5)

If it was with the same 2^{nd}-order temporal coherence of the excitation source, the laser pulse width, laser repetition rate, incident power, system collection efficiency, wavelength and working concentration, the action cross section of two-photon excitation ($\eta\sigma_2$) for a fluorophore as the reference compound is determined relative to the known action cross section, then the formula (5) is simplified as

$$(\eta\sigma_2)_2 = \frac{\text{counts}_2}{\text{counts}_1}(\eta\sigma_2)_1$$

(6)

, where sample 1 means the reference compound, and sample 2 means the fluorophore.

TPL of fluorescein and rhodamine B (Sigma Aldrich Co., USA) was needed to be verified. By measuring the dependence of the emission intensity on the excitation power range of 7.040 - 28.160 mW (from 704.0 nJ pixel^{-1} to 2816.0 nJ pixel^{-1}), the results were shown in **Fig. S17**†. The dependence was observed to be quadratic, with exponents of 1.99 (for fluorescein) and 2.01 (for rhodamine B) measured for increasing excitation power to determine the luminescence from TPE. In each figure, the slopes of the lines were to determine the fluorescence from two-photon process. Besides, for careful concern, the known action cross section of TPE for fluorescein (Sigma-Aldrich Co., USA) and rhodamine B (Sigma-Aldrich Co., USA) was firstly used as the standard reference and fluorophore to calculate each other's action cross section and *vice versa*. At 800 nm in wavelength of femtosecond laser exposure, the action cross section of TPE for fluorescein and rhodamine B is 36.4 and 153.0 GM (Goeppert–Mayer units, with 1 GM = 10^{-50} cm^4 s photon^{-1}),[9-12] respectively (also consider the free website http://www.drbio.cornell.edu/cross_sections.html, kindly provided by Prof. Chris Xu, Cornell University, USA). The integrated TPL intensity for "counts" was based on the spectra. Based on formula (6),[10] the TPE action cross section of fluorescein and rhodamine B could be calculated as 34.4 and 152.9 GM (**Table S1**†). Compared to the data in the previous studies, there is less than 5.5 % in error that is the acceptable deviation. In other words, the action cross section of TPE for sample was available *via* formula (5) and (6). Further, selected rhodamine B as a standard references[9-11] and the absolute cross sections of TPE for N-GQD and

N-GQD-polymers can be obtained, respectively, and showed in **Tables 1-2**. And there is no batch to batch variation for the materials in terms of two-photo properties.

Femtosecond laser optical system (for fluorescence lifetime imaging microscopy). Key components of our instrument/microscope include a femtosecond, titanium-sapphire (ti-sa) laser (Tsunami, Spectra-Physics, USA) with a pulse width of less than 100 fs and a repetition rate of 80 MHz, an inverted optical microscope (Axiovert 200, Zeiss, Germany), a x-y galvanometer scanner (6215H, Cambridge, USA), a triple-axis sample-positioning stage (ProScan^{TM}II, Prior, UK), a z-axis piezoelectric nano-positioning stage (Nano-F100, Mad City Labs, USA), an acousto-optic modulator (AOM) (23080-x-1.06-LTD, Neos, USA), PMTs (H5783P, Hamamatsu, Japan), and a data acquisition (DAQ) card with a field-programmable gate array (FPGA) module (PCI-7831R, National Instruments, USA). A detailed description of the multiphoton fabrication instrument can be found in our previous studies.[5,6] For fluorescence lifetime imaging microscopy (FLIM), the time-correlated single photon counting (TCSPC) module (PicoHarp 300, PicoQuant) is integrated into the main control platform based on LabVIEW programming, which triggers the synchronic signal via the FPGA module, collects the fluorescence time-to-digital data via a USB 2.0 interface, and then constructs the fluorescence lifetime image under LabVIEW. The time-to-digital data from different pixels is separated by inserting a marker signal from scanning synchronic trigger. To facilitate 3D lifetime image and data analysis, the LabVIEW program also records the scanning parameters corresponding to the time-to-digital data. The timer overflow signal of the TCSPC is removed, allowing the accumulated time-to-digital data of each pixel to form a histogram. Nonlinear least square algorithm is used to fit the fluorescence lifetime decay curve for each pixel. Based on the fitting lifetime data of each pixel and the pixel scanning information, the FLIM image can be displayed with a resolution of 0.1 ns under the main control platform. The lifetime data and the parameter generated by the triple-exponential equation fitting while monitoring the emission with 800 nm of wavelength under TPE (**Table S3**†).

Calculation of radiative and non-radiative decay rates.[13] PL QY and lifetime are both major parameters when investigating the emission characteristics of fluorescent dyes in diverse environments. The quantum yield Q can be expressed as

$$Q = \frac{\Gamma}{\Gamma + k} \tag{7}$$

, where Γ is the radiative decay rate and k is the non-radiative decay rate.

Fluorescence lifetime is usually defined as the average time required for an electron in the excited state to decay to the ground state. The TPL lifetime τ can be also relative to the decay rates and described as

$$\tau = \frac{1}{\Gamma + k} \tag{8}$$

Following Eq.(7) and (8), the radiative and non-radiative decay rates can be calculated.

Upon absorption of a photon, one of the weakly bound electrons of the fluorescent molecule—a fluorophore—is promoted to a higher energy level. The fluorophore is then said to be in an excited state, A^*. This state is metastable, and therefore the fluorophore will return to its stable ground state, A. It can do so either radiatively by emitting a fluorescence photon hv,

$$A^* \ -> \ A + hv$$

or non-radiatively, for example, by dissipating the excited state energy as heat

$$A^* \ -> \ A + \text{heat}$$

The depopulation of the excited state depends on the de-excitation pathways available. Fluorescence is the radiative deactivation of the lowest vibrational energy level of the first electronically excited singlet state, S_1, back to the electronic ground state, S_0. The singlet states are the energy levels that can be populated by the weakly bound electron without a spin flip. The absorption and emission processes are illustrated by an energy level diagram named after Aleksander Jablonski.

The fluorescence lifetime, τ, is the average time a fluorophore remains in the electronically excited state S_1 after excitation. τ is defined as the inverse of the sum of the rate parameters for all excited state depopulation processes: Eq. (8), where the non-radiative rate constant k is the sum of the rate constant for internal conversion, k_{ic}, and the rate constant for intersystem crossing to the triplet state, k_{isc}, so that $k = k_{ic}, + k_{isc}$. The fluorescence emission always occurs from the lowest vibrational level of S_1, a rule known as Kasha's rule, indicating that the fluorophore has no memory of its excitation pathway, e.g. one and two-photon excitation yields the same fluorescence spectrum, quantum yield and lifetime.

Cytotoxicity assay. 5×10^3 A431 cells per well in a 96-well culture plate were for overnight of incubation in the dark at 37°C with 5% CO_2 in air. All of N-GQD-Ab_{EGFR} and N-GQD-polymers-Ab_{EGFR} (delivered dose: 10-100 μg mL^{-1})

were respectively added to the incubated cells for overnight of incubation in the dark at 37°C. Remove and replace with the new culture medium and repeat for 3 to 5 times to wash out the nonspecific binding. The cells were collected by trypsinization, and a-10 min-centrifugation (1200 rpm) to collect the pellets. Then, follow the previous studies[14,15] to conduct the cytotoxicity assay (MTT assay) (Sigma-Aldrich Co., USA) with an ELISA reader (Thermo Electron, USA).

Reactive Oxygen Species (ROS) detection. ***For 1 day incubation.*** *Singlet oxygen ($^1O_2$).* (a) N-GQD-Ab_{EGFR} and N-GQD-polymers-Ab_{EGFR} were delivered at a dose from 10 to 70 μg mL^{-1}. Material-Ab_{EGFR}-treated-A431 cells (5×10^3) were respectively incubated for 4 h at 37 °C, and then 1 μM of Singlet Oxygen Sensor Green Reagent (SOSG) (Ex/Em: 488/525 nm)[16,17] (Invitrogen, USA) was added. Measurements were obtained using a PL spectrometer (F-7000, Hitachi, Japan). (b) N-GQD-Ab_{EGFR} and N-GQD-polymers-Ab_{EGFR} were delivered at a dose from 10 to 70 μg mL^{-1}. Material-Ab_{EGFR}-treated-A431 cells (5×10^3) were respectively incubated for 4 h at 37 °C, and then 10 μM of trans-1-(2′-methoxyvinyl)pyrene (*t*-MVP) (Thermo Fisher Scientific, USA)/ 0.1 M SDS (Sigma, USA) (Ex/Em: 352/465 nm)[18] was added in the dark. Reaction of *t*-MVP with $^1O_2$, yielding a dioxetane intermediate that generates fluorescence upon decomposition to 1-pyrenecarboxaldehyde. Furthermore, this highly selective fluorescent probe does not react with other activated oxygen species such as hydroxyl radical, superoxide or hydrogen peroxide. Measurements were obtained using a PL spectrometer. *Superoxide radical anion ($O_2^{\cdot-}$).* N-GQD-Ab_{EGFR} and N-GQD-polymers-Ab_{EGFR} were delivered at a dose from 10 to 70 μg mL^{-1}. Material-Ab_{EGFR}-treated-A431 cells (5×10^3 cells) were respectively incubated for 4 h at 37 °C, and mixed, incubated with 1 mL 0.45 mM 2,3-bis (2-methoxy-4-nitro-5-sulfophenyl)-2H-tetrazolium-5-carboxanilide (XTT) (Sigma-Aldrich Co., USA) for 5 h in the dark.[19] XTT would interact with superoxide radical anion and form the XTT-formazan showing strong absorption at 470 nm in wavelength. Measurement of absorption was recorded by UV-vis spectrometer (U-4100, Hitachi, Japan). Data are means ± SD (n = 6). *Glutathione (γ-L-glutamyl-L-cysteinyl-glycine, GSH) oxidation ($O_2^{\cdot-}$) (the Ellman's assay).* N-GQD-Ab_{EGFR} and N-GQD-polymers-Ab_{EGFR} were delivered in the concentration from 10 to 70 μg mL^{-1}. Material-Ab_{EGFR}-treated-A431 cells (5×10^3 cells) were respectively incubated overnight at 37 °C, and mixed, incubated with 50 mM bicarbonate buffer (pH 8.6) and GSH/0.8mM bicarbonate buffer in dark. Then, incubate in an incubator for 2 h at 37 °C. After this, the following experiments were according to the previous studies.[20-22] Loss of GSH (%) = (absorbance difference between of sample and negative control / absorbance of negative control) × 100 %.

For 4 day incubation. *Singlet oxygen ($^1O_2$).* (a) N-GQD-Ab_{EGFR} and

N-GQD-polymers-Ab_{EGFR} were delivered at a dose of 10 μg mL^{-1}. Material-Ab_{EGFR}-treated-A431 cells (5×10^3) were respectively incubated for 4 days at 37 °C, and then 1 μM of SOSG[16,17] was added. Measurements were obtained using a PL spectrometer. (b) N-GQD-Ab_{EGFR} and N-GQD-polymers-Ab_{EGFR} were delivered at a dose from 10 to 70 μg mL^{-1}. Material-Ab_{EGFR}-treated-A431 cells (5×10^3) were respectively incubated for 4 days at 37 °C, and then 10 μM of trans-1-(2′-methoxyvinyl)pyrene (*t*-MVP) (Thermo Fisher Scientific, USA)/ 0.1 M SDS (Sigma, USA) (Ex/Em: 352/465 nm)[18] was added in the dark. Reaction of *t*-MVP with $^1O_2$, yielding a dioxetane intermediate that generates fluorescence upon decomposition to 1-pyrenecarboxaldehyde. Furthermore, this highly selective fluorescent probe does not react with other activated oxygen species such as hydroxyl radical, superoxide or hydrogen peroxide. Measurements were obtained using a PL spectrometer. *Superoxide radical anion ($O_2^{\cdot-}$).* N-GQD-Ab_{EGFR} and N-GQD-polymers-Ab_{EGFR} were delivered at a dose of 10 μg mL^{-1}. Material-Ab_{EGFR}-treated-A431 cells (5×10^3 cells) were respectively incubated for 4 day at 37 °C, and mixed, incubated with 1 mL 0.45 mM XTT for 5 h in the dark.[19] XTT would interact with superoxide radical anion and form the XTT-formazan showing strong absorption at 470 nm in wavelength. Measurement of absorption was recorded by UV-vis spectrometer. *GSH oxidation ($O_2^{\cdot-}$) (the Ellman's assay).* N-GQD-Ab_{EGFR} and N-GQD-polymers-Ab_{EGFR} were delivered at a dose of 10 μg mL^{-1}. Material-Ab_{EGFR}-treated-A431 cells (5×10^3 cells) were respectively incubated for 4 days at 37 °C, and mixed, incubated with 50 mM bicarbonate buffer (pH 8.6) and GSH/0.8mM bicarbonate buffer in dark. Then, incubate in an incubator for 2 h at 37 °C. After this, the following experiments were according to the previous studies.[20-23] Loss of GSH (%) = (absorbance difference between of sample and negative control / absorbance of negative control) × 100 %. Data are means ± SD (n = 6).

TPL image. 5×10^3 A431 cells per well in a 96-well culture plate were for overnight of incubation in the dark at 37°C with 5% CO_2 in air. All of the N-GQD-Ab_{EGFR} and N-GQD-polymers-Ab_{EGFR} (delivered dose of material: 10 μg mL^{-1}.) were respectively added to the incubated cells to process the interaction of antibody-antigen for 2.5 h of incubation in the dark at 37°C. Remove and replace with the new culture medium and repeat for 3 to 5 times to wash out the nonspecific binding. The cells wee embedded in a collagen matrix to mimic the three-dimensional epithelium tissue. And the two-photon images of N-GQD-Ab_{EGFR}-, and N-GQD-polymers-Ab_{EGFR}-treated-A431 cells were observed using a nonlinear femtosecond laser microscopy optical system under TPE.

Uptake assay. A431 cells were incubated with 10 μg mL^{-1} N-GQD-PEI-PSS-Ab_{EGFR} and N-GQD-PEI-PSS, respectively. The absorbance of a quantity of 10 μg mL^{-1} materials was recorded by UV-vis spectroscopy (Abs: approximately 226 nm). The materials were mixed with A431 cells at 37 ℃ from 1h to 12h, respectively, centrifuge (1200 rpm) to remove excess materials, and keep the supernatant and measure its absorbance. The difference in absorbance between the collected supernatant and the original materials was estimated, resulting in the percentage of uptake at each time point.

And there is no batch to batch variation for the materials in terms of two-photo properties, two-photon photodynamic ability and two-photon contrast agents. Different optical system has different detection depth. Due to the detection efficiency and the objective we used, the maximal z depth we can observed by this laser optical system is around 100 μm. However, 93 μm in the work can show the optimal resolution in the mimic 3D biological specimens.

N-GQDs were prepared by an ultrasonic shearing reaction from graphene oxide sheets (**Fig. S2a†**). The diagram of height profile was determined by AFM, showing the image of a 0.83 ± 0.04 nm thick single layer of N-GQDs (**Fig. S2b†**). The typical thickness of a GQD with about a 0.4-0.7 nm increase in graphene thickness (~0.36 nm) was known due to the existence of hydroxyl, carboxyl and epoxy groups on two sides of the oxide surface. FTIR was used to analyze the exposed functional groups of N-GQD (**Fig. S2c†**). Results showed characteristic bands of N-GQDs for epoxy stretching about 1030 cm^{-1}, C－O stretching about 1118 cm^{-1}, phenolic C－OH stretching about 1213 cm^{-1}, tertiary alcoholic C－OH bending about 1365 cm^{-1}, symmetric carboxylate $C(=O)_2^-$, sp^2 C＝N and sp^3 C－N stretching about 1412, 1427 and 1436 cm^{-1}, C＝C ring stretching about 1628 cm^{-1}, C＝O stretching 1738 cm^{-1}, carboxylate O－H and N－H in-plane stretching 3218 and 3426 cm^{-1}. The results indicated the functional groups of carboxyl, hydroxyl and epoxy were exposed from N-GQDs. Results of UV-vis was indicative of N doping in GQDs successfully (**Fig. S2d†**). XPS was used to examine the surface chemistry of N-GQDs (**Fig. 1c-d**). After the annealing process, NH_3 would react with oxygen functional group of as-prepared graphene oxide to form C－N bonds. Atomic N decomposed from NH_3 could combine with defects sites of graphene oxide, resulting in the formation of the stable C－N bonding during high temperature.[24] Hence, the N structures of pyridine-N, pyrrolic-N and quaternary-N will be formed in N-doped graphene oxide under the annealing process. Then, the epoxy, hydroxyl and carboxyl groups will be shown in N-GQDs by the sequentially ultrasonic shearing oxidation reaction. The quantitative analysis determined the O(1s)/C(1s) atomic ratio for the N-GQDs is ca. 24.8 %, close to that of the GQDs (ca. 23.9 %) and higher than that of the graphene (ca. 14 %);[25-29] moreover, the N(1s)/C(1s) atomic ratio was around 4.9 % after calculation (**Fig. 1c-d**). The C－O bond may correspond to epoxy and tertiary alcohol functional groups on the basal plane, as well as phenol in the periphery. The C＝O and O－C＝O bonds indicate the presence of ketone and carboxylic groups in the graphene periphery. The C bonding composition reflected the fact that most of the oxygen functionalities were located on the graphene edge sites of the N-GQDs, as well as the percentages indicated that the N was mainly located in the graphene sheet edge. Results confirmed N-GQDs had been successfully oxidized from graphite and graphene oxide, represented the surface components of N-GQD in agreement with FTIR results and showing the incorporation of the pyridinic, pyrrolic and quaternary N atoms into the C backbone of GQDs. These functional groups make the N-GQDs soluble in water and keep stable without showing the appearance of precipitate in solution. The visible light PL emission occurs from the partial conjugated π electrons absorbed in the layered structure of N-GQDs,[30] as well as from the π-π* transition

between the aromatic N and the conjugate structure.[31,32] The PL peak shifts from 497 to 548 nm with the change of excitation wavelength from 410 to 500 nm, and the excitation wavelength-dependent emission was resulted from a larger conjugated π electrons system (a Stokes shift of about 87 nm for Ex/Em : 410 nm/ 497 nm, **Fig. S2e**†). The aforementioned characterisations confirmed that N-GQDs had been successfully synthesised.

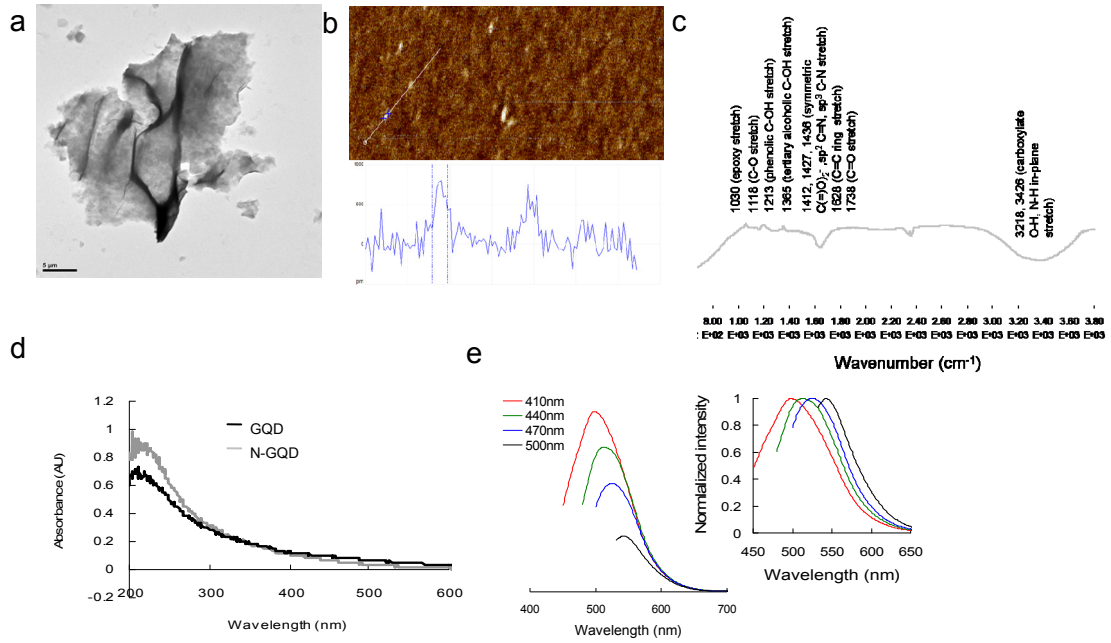

Fig. S2 (a) TEM image of graphene oxide. (b) AFM image of N-GQDs on mica, and the height difference between two arrows (the N-GQDs and mica) was 0.83 ± 0.04 nm. (c) FTIR spectrum of N-GQDs. (d) UV-vis spectra of GQDs and N-GQDs. (e) PL spectra of N-GQDs (inset: with the intensity normalized).

XRD, which was performed to analyze crystallinity, showed the diffraction angle of pristine graphite was about 26.20°, which indicates an interlayer distance of 0.342 nm; graphene oxide peaked at about 10.69°, which indicates the good layer regularity with a repeating interlayer distance of 0.835 nm; the small size of N-GQDs peaked broadly at about 24.41°, which means an interlayer distance of 0.358 nm (**Fig. S3**†). The distances between the lattice fringes are 0.358 nm and 0.214 nm (**Fig. 1a**), respectively, which are consistent with the in-plane lattice spacing and the basal plane distance of graphite. The XRD results suggested that there was no significant basal plane functionalization, which is consistent with our understanding that the graphenes have the much more active edges than the in-plane carbons, as well as the existence of functional groups at the edges of the N-GQDs. The value for a N-GQD is in agreement with values, 0.340–0.403 nm, reported for the N-GQD prepared with other methods[33,34] and the as-synthesized N-GQDs were confirmed to have a lamellar, well-ordered structure. The accommodation of various oxygen species, such as carboxyl, hydroxyl and epoxy groups, and changes in the carbon hexahedron grid plane that increase the spacing of the graphene layers result in the increased basal spacing of the N-GQDs.

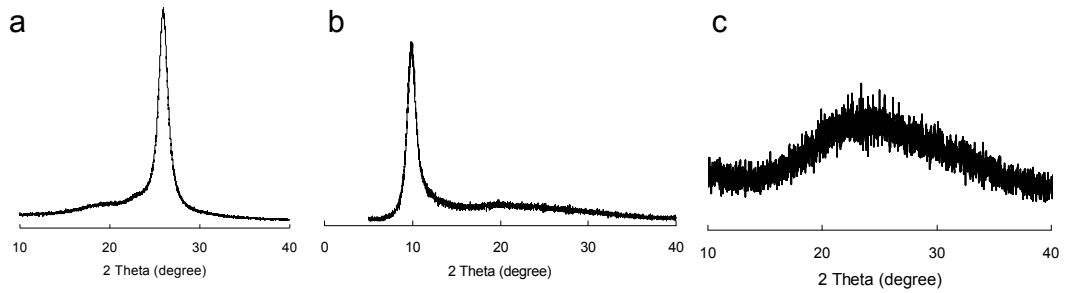

Fig. S3 XRD pattern used for analyzing the crystallinity of N-GQDs. The calculated interlayer distances of (a) graphite, (b) graphene oxide, and (c) N-GQDs were 0.342, 0.835, and 0.358 nm, respectively.

Raman spectroscopy was also used to examine the crystallinity of N-GQDs (**Fig. S4**†). The major feature bands of N-GQDs are the so-called G band (~1603 cm^{-1}), which comes from in-plane vibration in a two dimensional hexagonal lattice of sp^2 hybridized C－C bonds; the D band resulted from the defect, disorder, and sp^3-hybridized carbon in graphene layers by breaking the translational symmetry of the lattice occurred at about 1382 cm^{-1}. Results showed that the integrated intensity ratio of the D and G bands (I_D/I_G ratio), which represents the extent of disorder, was 0.85, that is much higher that that of graphite (0.105), clearly indicating higher distortion of N-GQDs. Besides, the initial graphene film has a I_D/I_G of 1.1,[28] which is reduced to 0.85 after oxidation reaction. This indirectly indicates that the defect sits within the graphene film have been preferentially attacked for the oxidation to break the starting reduced graphene oxide film into tiny pieces of less defects, and hence the observed reduced I_D/I_G, indicating the successful conversion from graphite, graphene oxide to N-GQDs.[29] Results show that the N incorporation will induce the generation of structural defect and the exposure of the edge planes, and oxygen-rich edges are formed in N-GQDs.

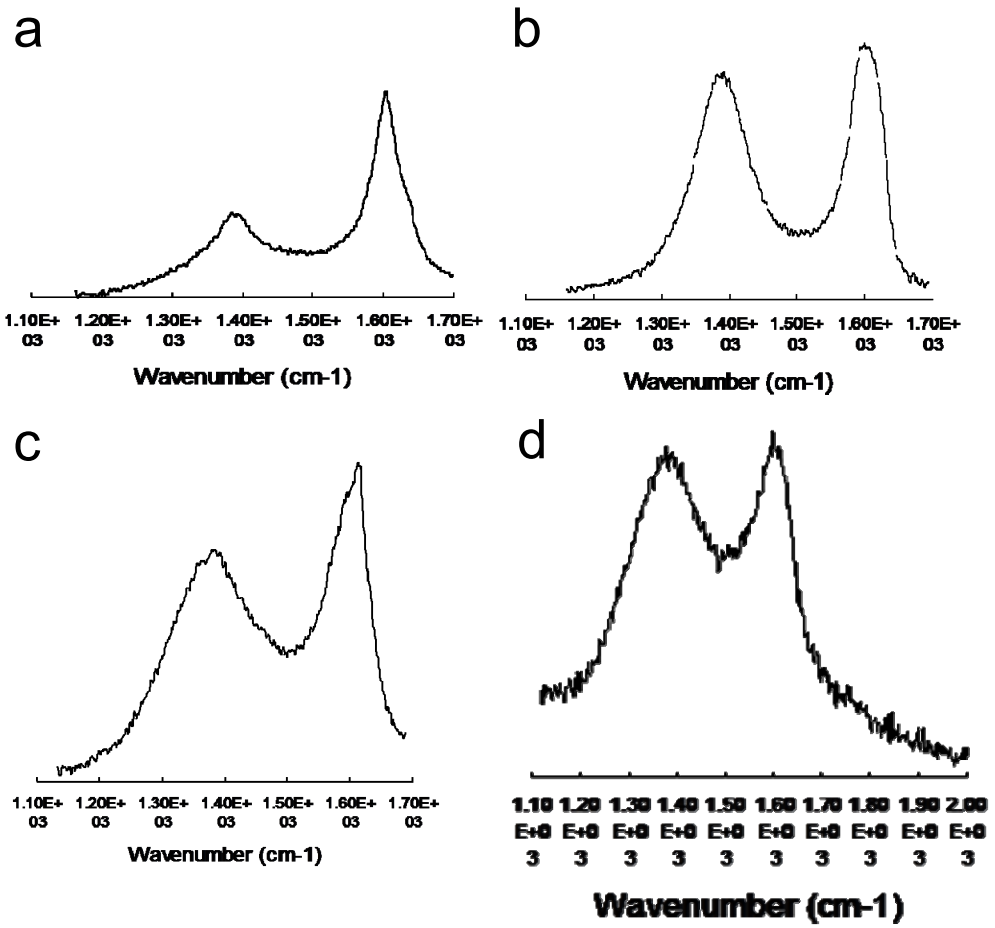

	D-band (cm^{-1})	G-band (cm^{-1})	I_D/I_G
graphite	1381	1602	0.105
graphene	1372	1610	1.1
gaphene oxide	1363	1601	1.02
N-GQD	1382	1603	0.85

Fig. S4 Raman spectra of (a) graphite, (b) graphene oxide, (c) graphene, and (d) N-GQDs. The data was summarized in the table.

The N-GQD-polymers had a relatively narrow size distribution ranging from 5 to 8 nm and magnification revealed that the interlayer spacing of 0.214 nm corresponded to the *d*-spacing of the graphene $\{1\bar{1}00\}$ lattice fringes, indicating the presence of graphene core in N-GQD (**Fig. S5**†).

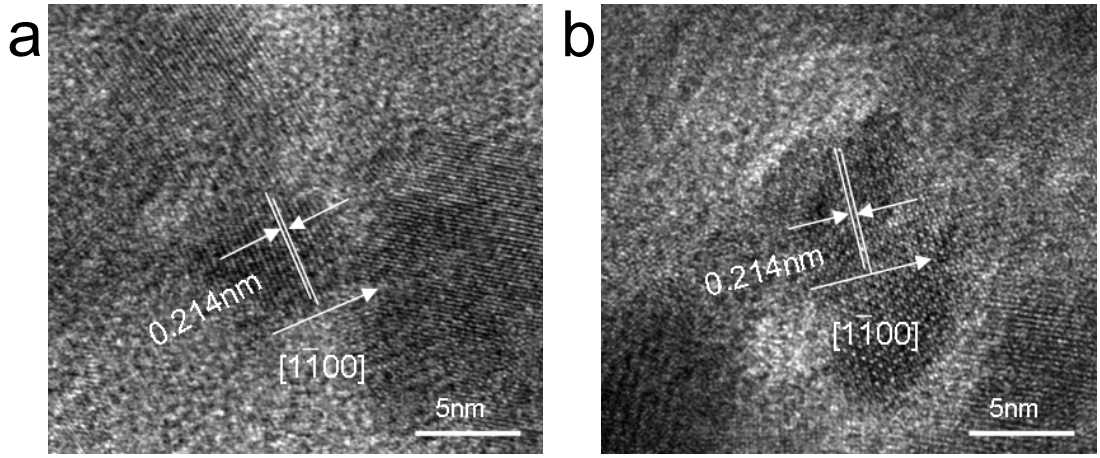

Fig. S5 TEM images of the (a) N-GQD-PEI and (b) N-GQD-PEI-PSS (Inset: single N-GQD). The lateral sizes of the N-GQD-polymers were between 5 and 8 nm of the mean lateral size.

AFM, 0.96 ± 0.03 nm thick, characteristic of a single of layer N-GQD-PEI (**Fig. S6a**†), which was dried on a mica surface, whereas one-layer N-GQD-PEI-PSS was 1.05 ± 0.05 nm thick (**Fig. S6b**†). Results showed PEI and PSS had been successfully adsorbed on the surface of the N-GQD via electrostatic interaction.

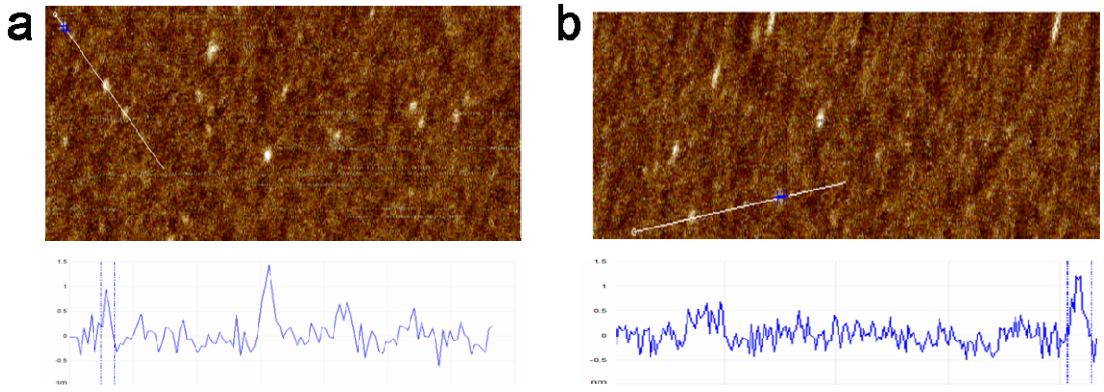

Fig. S6 AFM images of (a) N-GQD-PEI and (b) N-GQD-PEI-PSS on mica, respectively, and the height difference between two arrows (the N-GQD-based materials and mica) was 0.90-1.10 nm, consistent with the thickness of a single of layer N-GQD@polymers nanomaterial

FTIR was used to analyze the exposed functional groups of the N-GQD-polymers (**Fig. S7**†). Results showed characteristic bands of N-GQD-PEI for C－N stretching about 1042 cm^{-1} (band 1), C－H bending about 1301 cm^{-1} (band 2), broad N－H stretching 2352 cm^{-1} (band 3), C－H stretching about 2827 cm^{-1} (band 4), and N－H stretching 3302 cm^{-1} (band 5) (**Fig. S7a**†); the characteristic bands of N-GQD-PEI-PSS at approximately 1054 and 1134 cm^{-1} for C－N stretching (band 1 and 2), C－H bending about 1337 cm^{-1} (band 3), N－H bending about 1433 cm^{-1} (band 4), N－H bending and scissor about 1633 cm^{-1} (band 5), broad N－H stretching 2385 cm^{-1} (band 6), and primary sulfonamide 3323 cm^{-1} (band 7) (**Fig. S7b**†); the characteristic bands of PEI at approximately 1078 and 1127 cm^{-1} for C－N stretching (band 1 and 2), C－H bending about 1328 cm^{-1} (band 3), N－H bending about 1476 cm^{-1} (band 4), N－H bending and scissor about 1589 and 1683 cm^{-1} (band 5 and 6), broad N－H stretching 2339 cm^{-1} (band 7), C－H stretching about 2835 cm^{-1} (band 8), and N－H stretching 3318 cm^{-1} (band 9) (**Fig. S7c**†); the characteristic bands of PSS at approximately 843 cm^{-1} for C－H bending (band 1), in-plane C－H bending about 1013 and 1047 cm^{-1} (band 2 and 3), C－H bending about 1128, 1173 and 1409 cm^{-1} (band 4-6), ring C＝C stretching 1676 cm^{-1} (band 7), C－H stretching about 2924 cm^{-1} (band 8), and primary sulfonamide 3448 cm^{-1} (**Fig. S7d**†).

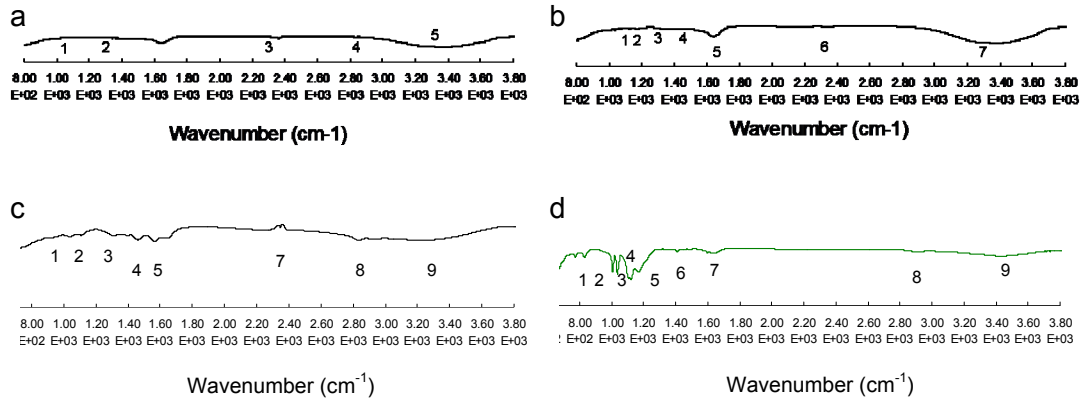

Fig. S7 FTIR spectra of (a) N-GQD-PEI, (b) N-GQD-PEI-PSS, (c) PEI and (d) PSS, respectively.

UV-vis spectrometer was used to confirm whether N-GQD-polymers were successfully synthesised and prepared. The N-GQD showed peaks at approximately 224 nm (π-π* transition of aromatic C＝C bonds) and 326 nm (n-π* transition of the C＝O shoulder and C－N). N-GQD-PEI exhibited absorptions at approximately 225 and 327 nm. N-GQD-PEI-PSS showed absorptions at approximately 228, and 325 nm, and peaked around 264 nm due to the coating of PSS (**Fig. S8**†).

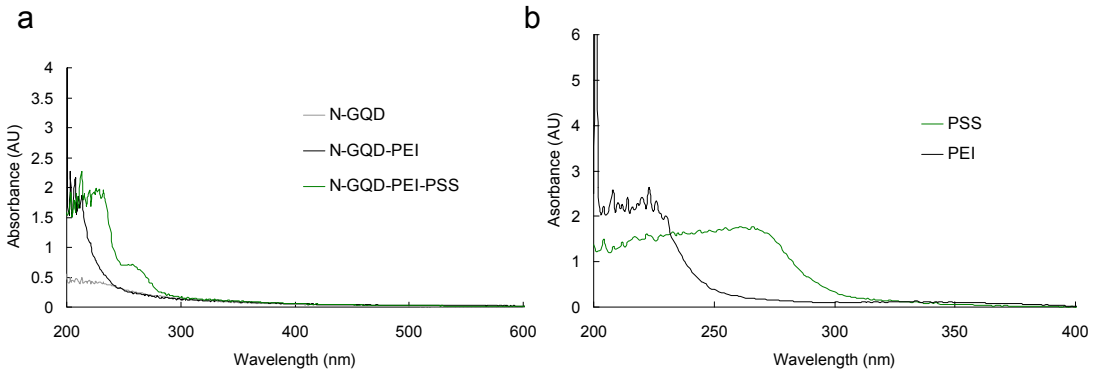

Fig. S8 UV-vis spectra of (a) N-GQD-PEI, N-GQD-PEI-PSS, and (b) polymers.

The crystallinity of N-GQDs had been examined by Raman spectroscopy and related discussion had been described in **Fig. S4**†. After the conjugation of PEI and PSS, in sequence, the position of the D band and G band shift from 1382 to 1352 cm^{-1} and from 1603 cm^{-1} to 1593 cm^{-1}, respectively (**Fig. S9**†). The I_D/I_G intensity ratios of N-GQD-PEI and N-GQD-PEI-PSS were 0.85 and 0.86, respectively. Probably because PEI and PSS are electron-donor molecules that cause high-frequency, tangential, vibrational modes of the carbon molecules in the N-GQD-polymers to shift to lower frequencies.[35]

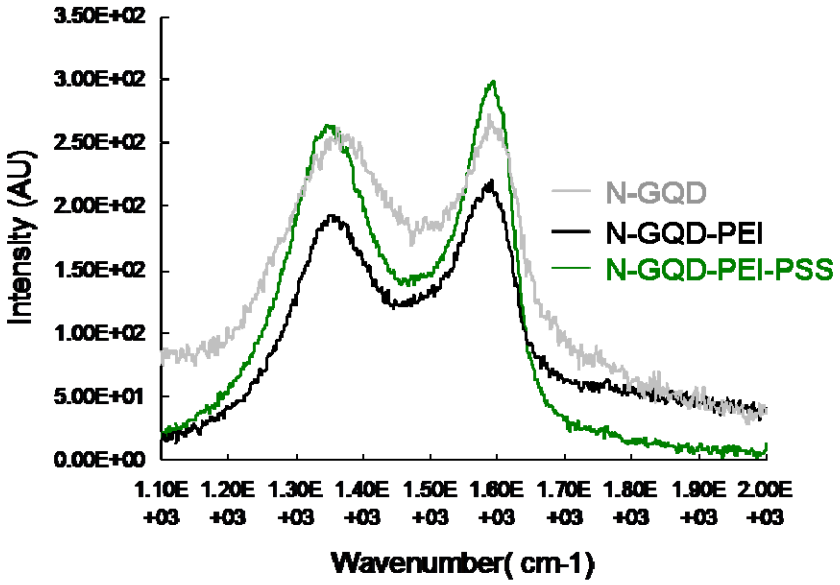

	D-band (cm^{-1})	G-band (cm^{-1})	I_D/I_G
N-GQD	1382	1603	0.85
N-GQD-PEI	1364	1596	0.85
N-GQD-PEI-PSS	1352	1593	0.86

Fig. S9 Raman spectra of N-GQDs, N-GQD-PEI, and N-GQD-PEI-PSS, respectively. The data was summarized in the Table.

Fig. S10† shows the PL spectra of N-GQD-based materials excited from 410 nm to 500 nm in wavelength by a PL spectrometer. For N-GQD, an emitted peak was observed around 497 nm and shifted to around 548 nm as the increase of excitation wavelength (**Fig. S10a†**). The PL intensity decreased and showed a red-shifted PL peak. Other PL spectra of N-GQD-polymers exhibited the similar trend in the same treatment (**Figs. S10b-c†**). Based on the results of XPS and FTIR (**Figs. 1c-d, S2c† and S7†**), the functional groups on the surface of the N-GQDs form surface states energy level between π and π* states of C＝C sp^2 clusters, which is influenced by the bandgap of σ and σ* states of the sp^3 matrix, are strongly confined.[36] Because of the difference in chemical bonding between C＝C and C＝O group, the variation of π* energy states is expected. Thus a distribution π* band (C＝C and C＝O) is resulted. And radiative recombination of electron-home pairs in such sp^2 clusters can arouse the fluorescence.[37] As shown in **Fig. S10d†**, the emission wavelength increases with the excitation in a linear relationship. The tunable PL can be explained in terms of surface states formed by the functional groups[38] at the surface of the N-GQDs. Further, the excitation wavelength dependence of the emission wavelength and intensity is a common phenomenon observed in carbon-based QD,[39,40] and implies both the size and surface state of those sp^2 clusters contained in N-GQDs were not uniform.[41] Beside, it was also suggested that emissive traps, electronic conjugated structure, and free zigzag sites are the main origin.[42,43] When the N-GQD-polymers were exposed by a excitation wavelength, a surface state emissive trap will dominates the emission. As the excitation wavelength changes, another corresponding surface state emissive trap will become dominant. As a result, the emissive traps induced by surface states of the functional groups should play an important role in the emission of N-GQD-polymers. This explains the excitation wavelength dependent phenomenon of N-GQD-polymers,[44] The red shift of the induced PL of N-GQDs is attributed mainly due to the appearance of graphitic (or quaternary) N. The newly-introduced energy level generated by the unique configuration of N (with different electronegativity) plays an important role in modulating the electrocatalytic activity, conduction type, conductivity and optical property. The structure-related properties make the N-GQD-polymers having stronger PL and higher QY to be an important fluorescent material.

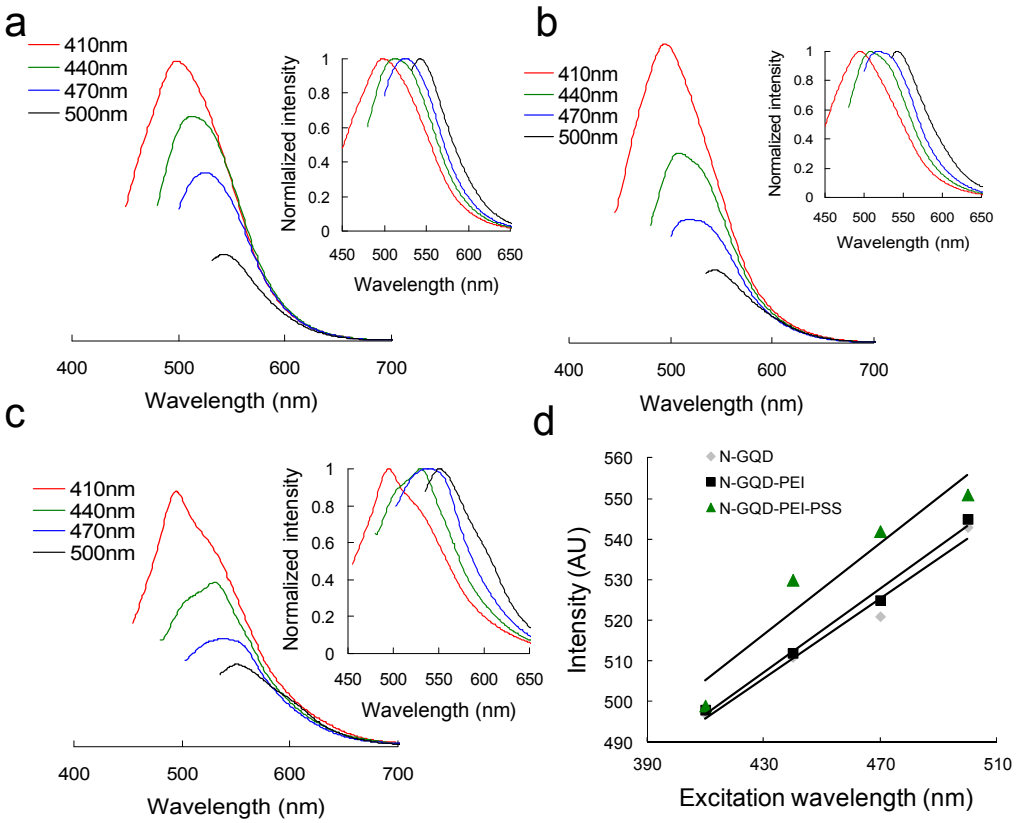

Fig. S10 PL spectra of the (a) N-GQDs (Ex: from 410 to 500 nm/ Em: from 497 to 548 nm), (b) N-GQD-PEI (Ex: from 410 to 500 nm/ Em: from 498 to 551 nm), (c) N-GQD-PEI-PSS (Ex: from 410 to 500 nm/ Em: from 501 to 556 nm) (inset: with the intensity normalized), and (d) almost direct proportion between the emission and excitation wavelength of the N-GQD-polymers, respectively.

XRD, which was performed to analyze crystallinity, showed the diffraction angle of N-GQD-PEI and N-GQD-PEI-PSS were about 24.42° and 24.44°, which indicates an interlayer distance of approximately 0.358 nm (**Fig. S11**†). Results implied that the polymer conjugations would not make any change to the interlayer distance of N-GQDs.

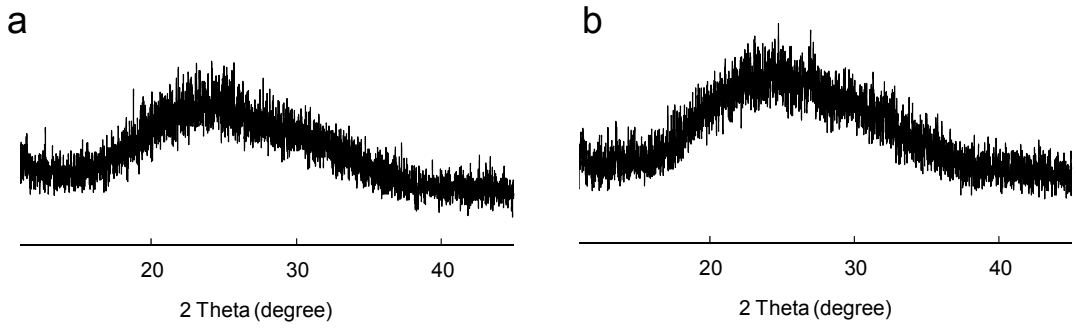

Fig. S11 XRD pattern used for analyzing the crystallinity of (a) N-GQD-PEI and (b) N-GQD-PEI-PSS.

Table. S1 Two-photon action cross sections of fluorescein (in 0.1 M NaOH, pH 11) and rhodamine B (in methanol). Excitation wavelength: 800 nm.

Excitation wavelength at 800 nm action cross section, $\eta\,\sigma 2$ (GM, $10^{-50}cm^4s/photon$)	Fluorescein (in ddH_2O, pH 11)	Rhodamine B (in methanol)
	34.4	152.9

Table. S2 TPE cross section of nanomaterials at 800 nm of excitation wavelength.[a]

Reference	Integrated emission intensity (counts)	Action cross-section ($\eta\ \sigma$)
Fluorescein	167.5	34.4

Sample	Integrated emission intensity (counts)	Relative quantum yield (η)	Absolute cross-section (σ)
Rhodamine B	744.5	0.69[b]	221.6
525 Qdot ITK carboxyl quantum dots (Q21341MP)	158171.4	0.81[c]	40103.9
565 Qdot ITK carboxyl quantum dots (Q21331MP)	157392.4	0.74[c]	43681.3

[a]Fluorescein was selected as the standard reference for the cross section (Information was from the free website http://www.drbio.cornell.edu/cross_sections.html, kindly provided by Prof. Chris Xu, Cornell University, USA), and the relevant calculations were shown in Experimental Section. [b]C. A. Parker and W. T. Rees, *Analyst,* 1960*,* **85**, 587-600. [c]Information was available in Thermo Fisher Scientific, USA.

Table. S3 The lifetime data and the parameter generated by the triple-exponential equation fitting while monitoring the emission with 800 nm of wavelength under TPE.[a]

	3 exp fitting model: (a0*exp (a1x)+a 2*exp(a 3x)+a4 *exp(a5 x)+a6)							lifetime 1	lifetime 2	lifetime 3	Ave lifetime (ns)
	a0	a1	a2	a3	a4	a5	a6				
N-GQD	6706.48	-5.54096	16459.8	-1.2774	8973.3	-0.31911	357.892	0.180474	0.78284	3.133725	1.313508053
N-GQD-PEI	871.468	-9.34981	3853.65	-1.69407	1517.87	-0.36617	88.4085	0.106954	0.590294	2.730957	1.043287721
N-GQD-PEI-PSS	4851.3	-16.2923	2286.39	-1.63486	725.957	-0.3534	28.6047	0.061379	0.611673	2.829631	0.476939022

[a]The parameters were obtained from the iterative reconvolution of the decay with the instrument response function.

As a function of TPE time (0-5 min), the relative intensity of integrated area from 400 nm to 680 nm in wavelength of TPL maintained almost the same intensity, exhibiting the highly photostability of N-GQD-PEI-PSS (**Fig. S12**†).

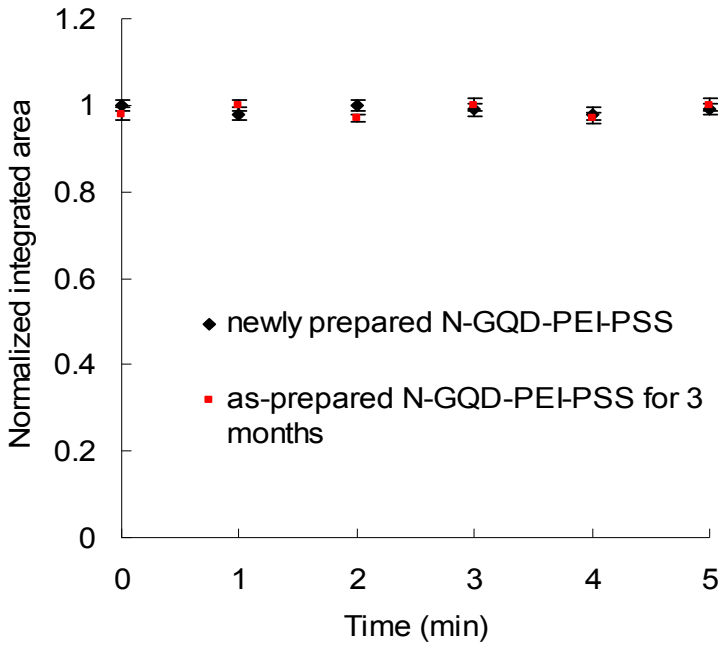

Fig. S12 Photostability of N-GQD-PEI-PSS, which was subjected to TPE at 1.760 mW (176.0 nJ pixel^{-1}) for 5 min (Ex: 800 nm/ Em: 596 nm). Other emission

intensities of integrated area after photoexcitation were respectively divided into that of newly prepared N-GQD-PEI-PSS without photoexcitation, leading to obtain the normalized integrated area. Delivered dose of material: 10 μg mL^{-1}. Data shown are means ± SD (n = 6).

Table. S4 Stability of the newly prepared-N-GQD-PEI-PSS and as-prepared N-GQD-PEI-PSS for 3 months in physiological environment of the culture medium for A431 cancer cell determined by DLS and zeta potential spectroscopy.

Newly prepared	Mean lateral size (nm)	Zeta potential (mV)
ddH_2O	6.9 ± 1.0 nm	- 18.2
PBS	6.9 ± 1.3 nm	- 19.3
Culture medium (for A431 cell)	7.0 ± 1.2 nm	- 19.6
As-prepared for 3 months	**Mean lateral size (nm)**	**Zeta potential (mV)**
ddH_2O	6.9 ± 1.2 nm	- 18.6
PBS	7.0 ± 1.1 nm	- 19.1
Culture medium (for A431 cell)	6.9 ± 1.4 nm	- 19.4

Considering the false positive signals of ROS might have resulted from the interactions between the materials and ROS reagents SOSG Reagent, XTT which led to the results being compromised,[45] the results showed that the N-GQD and N-GQD-polymers had the ability of generation of nonreactive oxygen species-dependent oxidative stress (**Fig. S13**†).

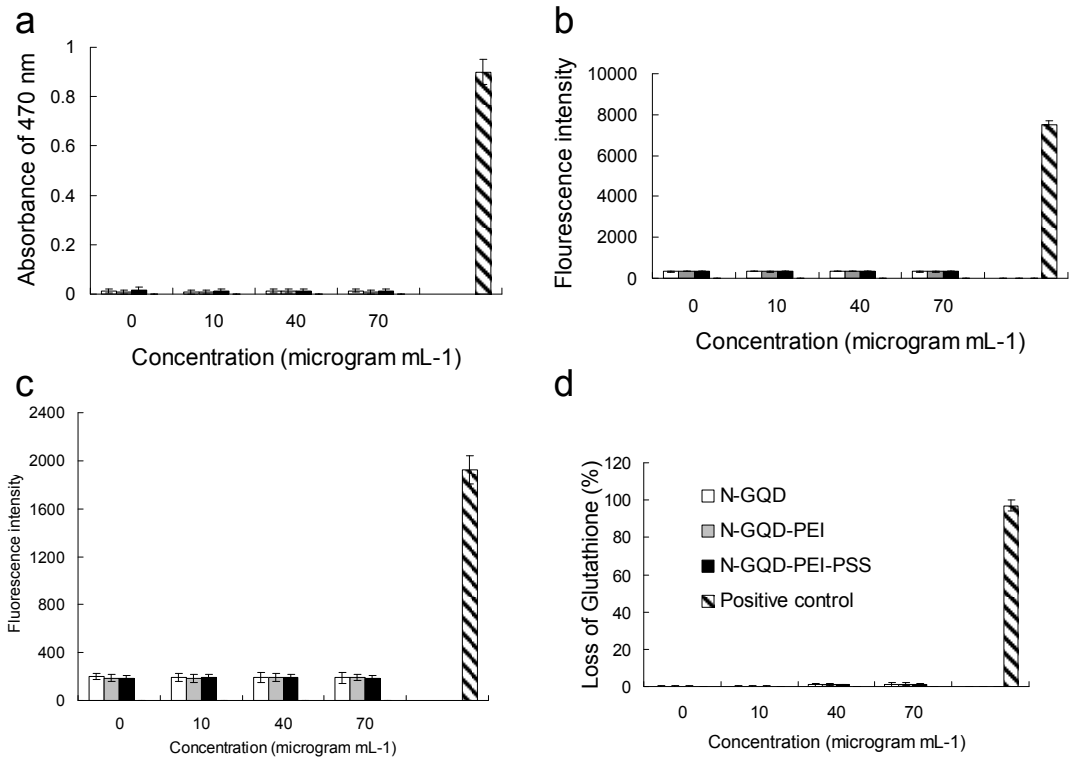

Fig. S13 (a) N-GQD and N-GQD-polymers were mixed with SOSG Reagent, respectively, and singlet oxygen ($^1O_2$) was generated. SOSG was used to detect $^1O_2$ with a PL spectrophotometer (Ex/Em: 488/525 nm). (b) N-GQD and N-GQD-polymers were mixed with *t*-MVP, respectively, and singlet oxygen ($^1O_2$) was generated. *t*-MVP can react with $^1O_2$, forming a dioxetane intermediate that generates fluorescence upon decomposition to 1-pyrenecarboxaldehyde, and monitored by a PL spectrometer (Ex/Em: 352/465 nm). (c) N-GQD and N-GQD-polymers were mixed with XTT, respectively, and superoxide radical anion ($O_2^{\cdot-}$) was generated. XTT was used to monitor the generated $O_2^{\cdot-}$ and record the absorbance at 470 nm. (d) N-GQD and N-GQD-polymers were mixed with GSH. GSH containing a thiol-tripeptide can prevent damages to cellular or bacterial components caused by stress of oxidation. Thiol group from GSH can be oxidized to disulfide bond converting GSH to glutathione disulfide. GSH oxidation was used to

determine the generated $O_2^{\cdot-}$. Positive control: the treatments of 50 μM *tert*-butyl hydroperoxide (TBHP)[46] and each reagent. Data shown are means ± SD (n = 6).

N-GQDs and N-GQD-polymers displayed high biocompatibility by MTT assay for 24 h of incubation, as well as ROS assays (**Fig. S14**†). Even though after 4-day incubation, results showed the same biocompatibility (**Fig. S15**†). These determinations showed that the N-GQDs and N-GQD-polymers did not induce any oxidative stress at any concentration, reflecting high biocompatibility.

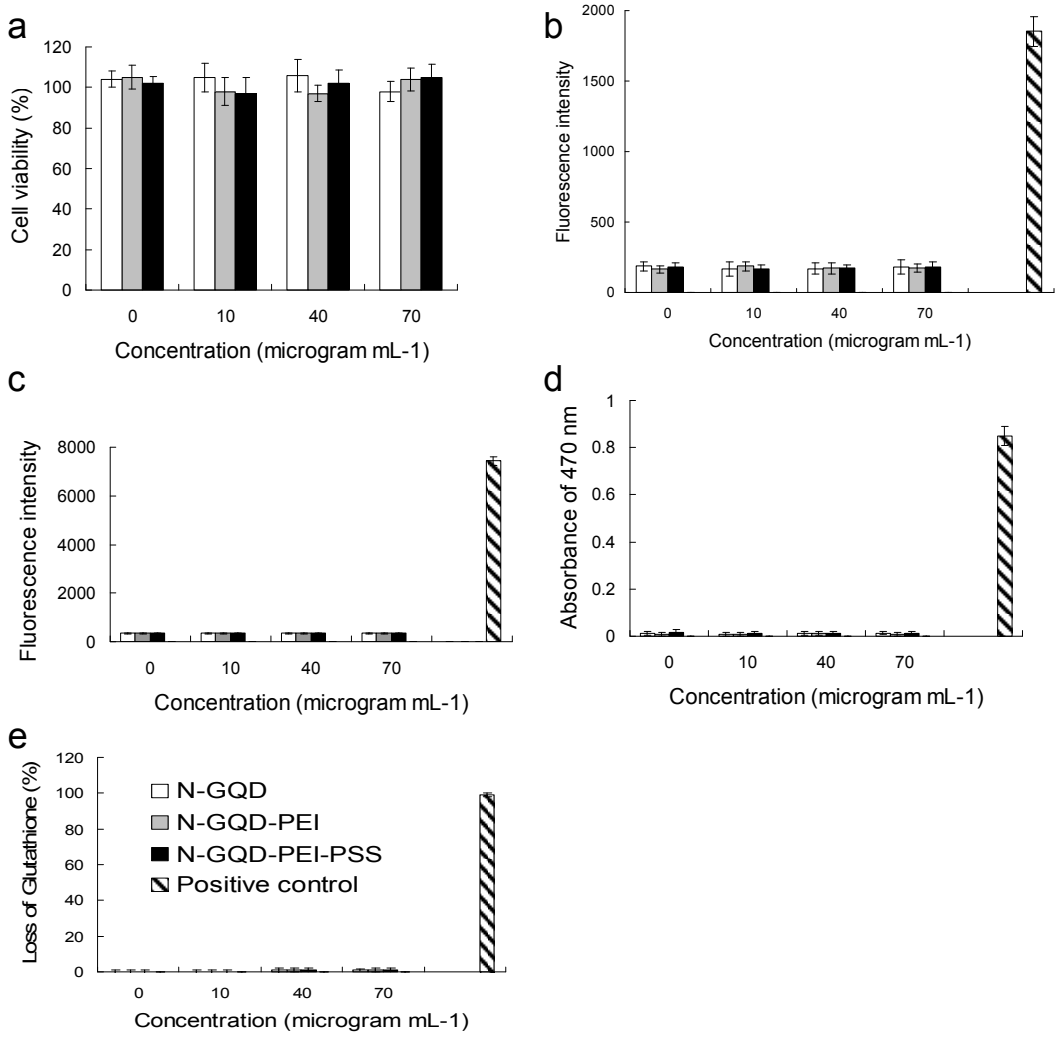

Fig. S14 (a) Estimation of the viability (24 hours) of the N-GQD-Ab_{EGFR}- and N-GQD-polymers-Ab_{EGFR}-treated A431 cells. (b) SOSG Reagent and (c) *t*-MVP were used to detect singlet oxygen ($^1O_2$), respectively. Measurements of $^1O_2$ were conducted by monitoring the N-GQD-Ab_{EGFR}- and N-GQD-polymers-Ab_{EGFR}-treated A431 cells. (d) After A431 cells were treated with N-GQD-Ab_{EGFR} and N-GQD-polymers-Ab_{EGFR}, superoxide radical anion ($O_2^{\cdot-}$) was generated. XTT was used to monitor the generated $O_2^{\cdot-}$ and record the absorbance at 470 nm. (e) GSH was

used to monitor the oxidative stress of the N-GQD-Ab_{EGFR}- and N-GQD-polymers-Ab_{EGFR}-treated A431 cells (dose of materials delivered: 0–70 μg mL^{-1}). Positive control: the treatments of 50 μM TBHP[46] and each reagent. Data shown are means ± SD (n = 6).

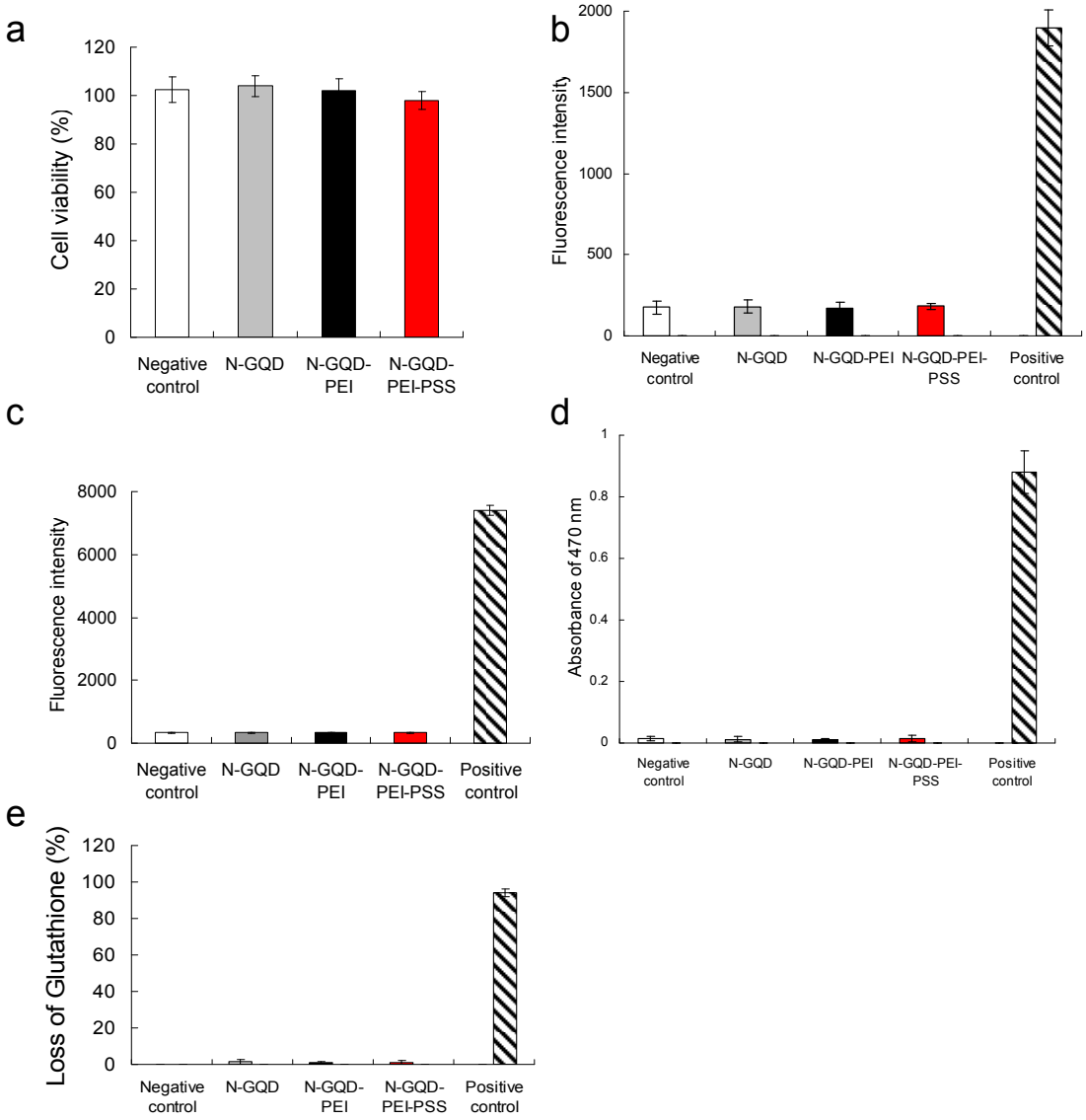

Fig. S15 (a) Estimation of the viability (4 days) of the N-GQD-Ab_{EGFR}- and N-GQD-polymers-Ab_{EGFR}-treated A431 cells. (b) SOSG Reagent and (c) *t*-MVP were used to detect singlet oxygen ($^1O_2$), respectively. Measurements of $^1O_2$ were conducted by monitoring the N-GQD-Ab_{EGFR}- and N-GQD-polymers-Ab_{EGFR}-treated A431 cells. (d) After A431 cells were treated with N-GQD-Ab_{EGFR} and N-GQD-polymers-Ab_{EGFR}, superoxide radical anion ($O_2^{\bullet-}$) was generated. XTT was used to monitor the generated $O_2^{\bullet-}$ and record the absorbance at 470 nm. (e) GSH was used to monitor the oxidative stress of the N-GQD-Ab_{EGFR}- and

N-GQD-polymers-Ab_{EGFR}-treated A431 cells (delivered dose of material: 10 μg mL^{-1}). Negative control: no materials and only reagent delivery. Positive control: the treatments of 50 μM TBHP[46] and each reagent. Data shown are means ± SD (n = 6).

The TPE induced temperature change of N-GQD and N-GQD-PEI-PSS. The temperature elevated curve as a function of irradiation time (0-20 s) from the both nanomaterials showing the similar trend to water, no obvious elevation of temperature (**Fig. S16†**)

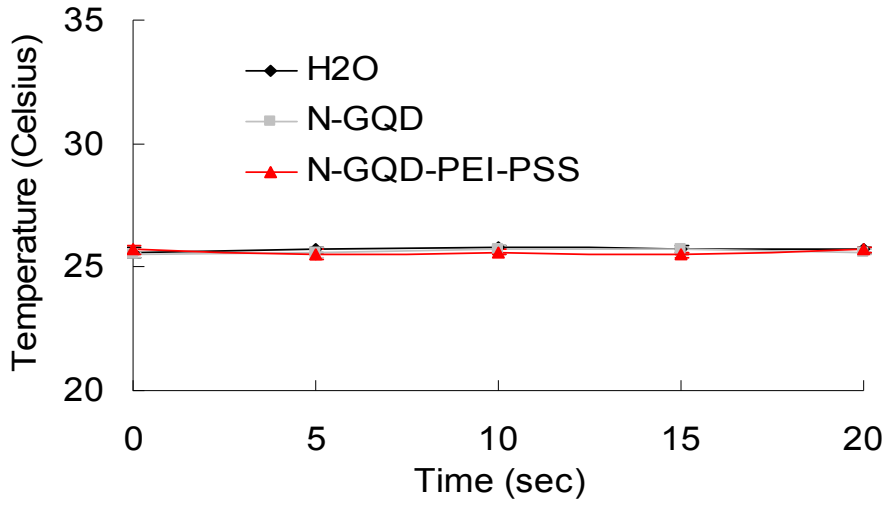

Fig. S16 The temperature dependences of N-GQD and N-GQD-PEI-PSS as a function of irradiation time at a power density of 2.974 mW (297.4 nJ $pixel^{-1}$) under TPE. Delivered dose: 10 μg mL^{-1} nanomaterials. Data are means ± SD (n=5).

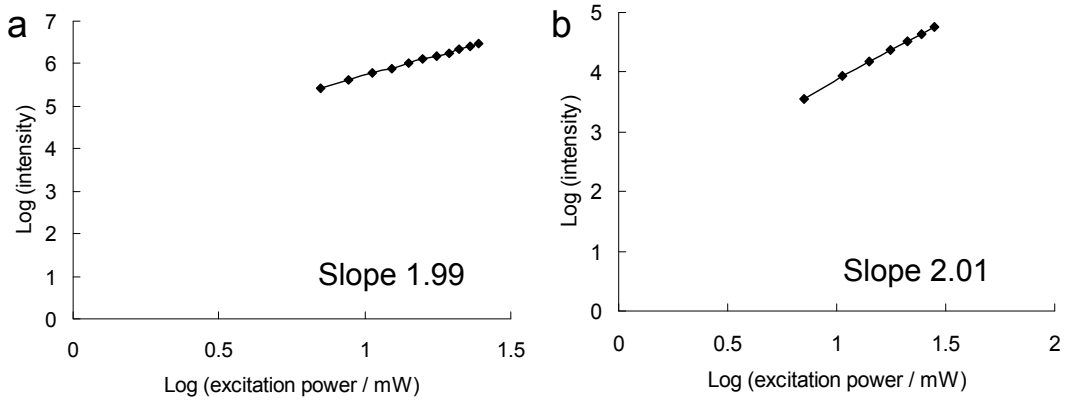

Fig. S17 Logarithmic plat of TPL intensity as a function of TPE from 7.040 to 28.160 mW (from 704.0 nJ $pixel^{-1}$ to 2816.0 nJ $pixel^{-1}$). (a) Fluorescein (in 0.1M NaOH, pH 11) with a slope of 1.99 and (b) rhodamine B (in methanol) with a slope of 2.01. R^2 > 0.99. Excitation wavelength: 800 nm.

References

1 W. S. Hummers and R. E. Offeman. *J. Am. Chem. Soc.,* 1958, **80**, 1339.

2 D. M. Togashi, B. Szczupak, A. G. Pyder, A. Calvet and M O'Loughlin, *J. Phys. Chem. A.,* 2009, **113**, 2757-2767.

3 R. Sjoback, J. Nygren and M. Kubista, *Spectrochimica. Acta A.,* 1995, **51**, L7-L21.

4 C. Würth, M. Grabolle, J. Pauli, M. Spieles and U. Resch-Genger. *Nat. Protoc.,* 2013, **8**, 1535-1550.

5 W. S. Kuo, C. H. Lien, K. C. Cho, C. Y. Chang, C. Y. Lin, L. L. H. Huang, P. J. Campagnola, C. Y. Dong and S. J. Chen, *Opt. Express,* 2010, **18**, 27550-27559.

6 C. H. Lien, W. S. Kuo, K. C. Cho, C. Y. Lin, Y. D. Su, L. L. Huang, P. J. Campagnola, C. Y. Dong and S. J. Chen, *Opt. Express,* 2011, **19**, 6260-6268.

7 H. Wang, T. B. Huff, D. A. Zweifel, W. He, P. S. Low, A. Wei and J. X. Cheng, *Proc. Natl. Acad. Sci. USA,* 2005, **102**, 15752-15756.

8 G. Zhou and M. Gu, *Opt. Lett.,* 2006, **31**, 2783-2785.

9 C. Xu, W. Zipfel, J. B. Shear, R. M. Williams and W. W. Webb, *Proc. Natl. Acad. Sci. USA,* 1996, **93**, 10763-10786.

10 L. C. Cheng, N. G. Horton, K. Wang, S. J. Chen and C. Xu, Biomed. *Opt. Express,* 2014, **5**, 3427-3433.

11 C. Xu and W. W. Webb, J. Opt. Soc. Am. B, 1996, 13, 481-491.

12 N. J. Durr, T. Larson, D. K. Smith, B. A. Korgel, K. Sokolov and A. Ben-Yakar, *Nano Lett.,* 2007, **7**, 941-945.

13 J. R. Lakowicz, *3rd. Edition. Springer.,* 2010.

14 W. S. Kuo, S. M. Hwang, H. T. Sei, Y. C. Ku, L. F. Hsu, P. C. H. Hsieh and C. S. Yeh, *J. Chin. Chem. Soc.,* 2009, **56**, 940-948.

15 W. S. Kuo, Y. C. Ku, H. T. Sei, F. Y. Cheng and C. S. Yeh, *J. Chin. Chem. Soc.,* 2009, **56**, 923-934.

16 W. S. Kuo, C. N. Chang, Y. T. Chang and C. S. Yeh. C.. *Chem. Commun.,* 2009, 4853-4855.

17 W. S. Kuo, C. N. Chang, Y. T. Chang, M. H. Yang, Y. H. Chien, S. J. Chen and C. S. Yeh. *Angew. Chem. Int. Ed.,* 2010, **49**, 2711-2715.

18 A. Thompson, J. R. Lever, K. A. Canella, A. Miura, G. H. Posner and H. H. Seliger. *J. Am. Chem. Soc.,* 1986, **108**, 4498-4504.

19 S. Liu, T. H. Zeng, M. Hofmann, E. Burcombe, J. Wei, R. Jiang, J. Kong and Y. Chen, Y. *ACS Nano,* 2011, **5**, 6971-6980.

20 S. Park, N. Mohanty, J. W. Suk, A. Nagaraja, J. Q. R. D. Piner, W. Cai, D. R. Dreyer, V. Berry and R. S. Ruoff. *Adv. Mater.,* 2010, **22**, 1736-1740.

21 O. Carmel-Hare and G. Storz, *Annu. Rev. Microbiol.,* 2000, **54**, 439.

22 G. L. Ellman, *Arch. Biochem. Biophys.,* 1959, **82**, 70.
23 F. Ren, S. Bhana, D. D. Norman, J. Johnson, J. Xu, D. L. Baker, A. L. Parrill and X. Huang. *Bioconjugate Chem.,* 2013, **24**, 376−386.
24 B. Guo, Q. Liu, E. Chen, H. Zhu, L. Fang and J. R. Gong. *Nano Lett.,,* 2010, **10**, 4975–4980.
25 T. F. Yeh, C. Y. Teng, S. J. Chen and H. Teng, *Adv. Mater.,* 2014, **26**, 3297-3303.
26 N. R. Wilson, P. A. Pandey, R. Beanland, R. J. Young, I. A. Kinloch, L. Gong, Z. Liu, K. Suenaga, J. P. Rourke , S. J. York and J. Sloan. *ACS Nano,* 2009, **3** , 2547-2556.
27 T. V. Khai, H. G. Na, D. S. Kwak, Y. J. Kwon, H. Ham, K. B. Shim and H. W. Kim. *Carbon,* 2012, **50**, 3799-3806.
28 Y. Li, Y. Zhao, H. Cheng, Y. Hu, G. Shi, L. Dai and L. Qu, *J. Am. Chem. Soc.,* 2012, **134**, 15-18.
29 X. Dong, C. Y. Su, W. Zhang, J. Zhao, Q. Ling, W. Huang, P. Chen, L. J. Li. *Phys. Chem. Chem. Phys.* 2010, **12,** 2164–2169.
30 L. Tang, R. Ji, X. Li, G. Bai, C. P. Liu, J. Hao, K. S. Teng, Z. Yang and S. P. Lau. *ACS Nano* 2014, **8**, 6312−6320.
31 J. Sun, S. Yang, Z. Wang, H. Shen, T. Xu, L. Sun, H. Li, W. Chen, X. Jiang, G. Ding, Z. Kang, X. Xie and M. Jiang. *Part. Part. Syst. Charact.* 2015, **32**, 434-440.
32 X. Deng, J. Sun, S. Yang, H. Shen, W. Zhou, J. Lu, G. Ding and Z. Wang. *Appl. Phys. Lett.* 2015, **107**, 241905-1-241905-4.
33 G. Eda, Y. Y. Lin, C. Mattevi, H. Yamaguchi, H. A. Chen, I. S. Chen, C. W. Chen and M. Chhowalla. *Adv. Mater.* 2010, **22**, 505–509.
34 K. P. Loh, Q. Bao, G. Eda and M. Chhowalla, *Nat. Chem.,* 2010, **2**, 1015-1024.
35 A. M. Rao, P. C. Eklund, S. Banbow, A. Thess and R. E. Smalley, *Science,* 1997, **388**, 257-259.
36 S. Zhu, J. Zhang, C. Qiao, S. Tang, Y. Li, W. Yuan, B. Li, L. Tian, F. Liu, R. Hu, H. Gao, H. Wei, H. Zhang, H. Sun and B. Yang, *Chem. Commun.,* 2011, **47**, 6858-6860.
37 C. T. Chien, S. S. Li, W. J. Lai, Y. C. Yeh, H. A. Chen, I. S. Chen, *Angew. Chem. Int. Ed.,* 2012, **51**, 6662-6666
38 C. M. Luk, B. L. Chen, K. S. Teng, L. B. Tang and S. P. Lau. *J. Mater. Chem. C,* 2014, **2**, 4526-4532.
39 D. Y. Pan, J. C. Zhang, Z. Li and M. H. Wu, *Adv. Mater.,* 2010, **22**, 734-738.
40 J. Shen, Y. Zhu, C. Chen, X. Yang and C. F. Li, *Chem. Commu.,* 2011, **47**, 2580-2582.

41 S. Chen, X. Hai, C. Xia, X. W. Chen and J. H. Wang. *Chem. Eur. J.,* 2013, **19**, 15918-15923.

42 Y. Li, Y. Hu, Y. Zhao, G. Shi, L. Deng, Y. Hou and L. Qu, *Adv. Mater.,* 2011, **23**, 776-780.

43 R. Liu, D. Wu, X. Feng and K. Müllen, *J. Am. Chem. Soc.*, 2011, **133**, 15221-15223.

44 L. Tang, R. Ji, X. Cao, J. Lin, H. Jiang, X. Li, K. S. Ten, C. M. Luk, S. Zeng, J. Hao and S. P. Lau, *ACS Nano,* 2012, **6**, 5102-5110.

45 D. Y. Lyon, L. Brunet, G. W. Hinkal, M. R. Wiesner and P. J. J. Alvarez. *Nano Lett.,* 2008, **8**, 1539-1543.

46 H. Possel, H. Noack, W. Augustin, G. Keilhoff and G. Wolf. *FEBS Lett.,* 1997, **416**, 175-178.